1   **Formation and sink of glyoxal and methylglyoxal in a polluted subtropical**
2   **environment: observation-based photochemical analysis and impact evaluation**

3   Zhenhao Ling[1], Qianqian Xie[2], Zhe Wang[3,4]*, Tao Wang[5], Hai Guo[5], Xuemei Wang[2,4]*
4   [1.] School of Atmospheric Sciences, Sun Yat-sen University, Guangzhou, China
5   [2.] Institute for Environmental and Climate Research, Jinan University, Guangzhou, China
6   [3.] Division of Environment and Sustainability, The Hong Kong University of Science and
7   Technology, Hong Kong, China
8   [4.] Guangdong-Hongkong-Macau Joint Laboratory of Collaborative Innovation for
9   Environmental Quality, Guangzhou, China
10 [5.] Department of Civil and Environmental Engineering, Hong Kong Polytechnic University,
11 Hong Kong, China
12 *Correspondence: Zhe Wang (z.wang@ust.hk) and Xuemei Wang (eciwxm@jnu.edu.cn)

13

14 **Abstract**

15 The dicarbonyls, glyoxal (Gly) and methylglyoxal (Mgly) have been recognized as

16 important precursors of secondary organic aerosols (SOAs) through the atmospheric

17 heterogeneous process. In this study, field measurement was conducted at a receptor

18 site in the Pearl River Delta (PRD) region in south China, and an observation based

19 photochemical box model was subsequently applied to investigate the production and

20 evolution of Gly and Mgly as well as their contributions to SOA formation. The model

21 was coupled with a detailed gas-phase oxidation mechanism of volatile organic

22 compounds (VOCs) (*i.e.,* MCM v3.2), heterogeneous processes of Gly and Mgly (*i.e.*,

23 reversible partitioning in aqueous phase, irreversible volume reactions and irreversible

24 surface uptake processes), and the gas-particle partitioning of oxidation products. The

25 results suggested that without considering the heterogeneous processes of Gly and

26 Mgly on aerosol surfaces would overpredict the mixing ratios of Gly and Mgly by

27 factors of 3.3 and 3.5 compared to the observed levels. The agreement between

28 observation and simulation improved significantly when the irreversible uptake and the

29 reversible partitioning were incorporated into the model, which in total contributed ~72

30 and ~73% to the destruction of Gly and Mgly, respectively. Further analysis on the

31 photochemical budget of Gly and Mgly showed that the oxidation of aromatics by the

32 OH radical was the major pathway producing Gly and Mgly, followed by degradation

33 of alkynes and alkenes. Furthermore, based on the improved model mechanism, the

34 contributions of VOCs oxidation to SOA formed from gas-particle partitioning (SOA_{gp})

35 and from heterogeneous processes of Gly and Mgly (SOA$_{het}$) were also quantified. It

36 was found that *o*-xylene was the most significant contributor to SOA$_{gp}$ formation

37 (~29%), while *m/p*-xylene and toluene made dominant contributions to SOA$_{het}$

38 formation. Overall the heterogeneous processes of Gly and Mgly can explain ~21% of

39 SOA mass in the PRD region. The results of this study demonstrated the important roles

40 of heterogeneous processes of Gly and Mgly in SOA formation, and highlighted the

41 need for a better understanding of the evolution of intermediate oxidation products.

42

43 **Keywords:** Glyoxal, Methylglyoxal, Secondary organic aerosol, Pearl River Delta,

44 Volatile organic compound, Photochemical box-model

45

46 **1. Introduction**

47   Organic aerosols (OAs) are important components of atmospheric aerosols, with

48 important impacts on radiation balance, air quality, atmospheric oxidative capacity, and

49 climate change (Zhu et al., 2011; Carlton et al., 2009; Hoyle et al., 2009). In addition

50 to the primary organic components (primary OA, POA) directly emitted from various

51 sources in the particulate form, a large fraction of OAs are secondarily produced (SOA)

52 through the aging of POAs, and through complex homogenous/heterogeneous reactions

53 of volatile or semi-volatile organic compounds (VOCs, SVOCs) (Jimenez et al., 2009;

54 Steinfeld and Jeffrey, 1998). SOA has frequently been observed to dominate the OA in

55 many regions, particularly during severe haze pollution events (Guo et al., 2012; Zhang

56 et al., 2017). However, the characteristics of SOAs are still poorly understood because

57 of their complicated formation mechanisms, various chemical compositions, and

58 multitude of precursors from diverse emissions, thus making SOAs an important

59 research topic in the field of the atmospheric environment.

60   In addition to primary precursors including isoprene, terpene and aromatic

61 hydrocarbons, glyoxal (Gly) and methylglyoxal (Mgly) have been recognized to be of

62 critical importance to SOA formation, especially through heterogeneous and multiphase

63 processes, in many laboratory and model studies (Waxman, et al., 2013, 2015; McNeill

64 et al., 2012; De Haan et al., 2009; Fu et al., 2008). Many efforts have been made to

65 investigate the sources, evolution of Gly and Mgly and their contributions to SOA

66 (Benavent et al., 2019; Zhang et al., 2016; Sumner et al., 2014; DiGangi et al., 2012;

67 Stavarakou et al., 2009). As two smallest dicarbonyl compounds, the sources of Gly

68 and Mgly are complicated. The burning of biomass and biofuel combustion have been

69 considered as the primary emission sources of Gly and Mgly, although recent studies

70 have identified that vehicular emissions are also primary sources of these pollutants

71 (Grosjean et al., 2001; Zhang et al., 2016). Compared with primary emissions,

72 secondary formations from the oxidation of volatile organic compounds (VOCs) make

73 more dominant contributions to ambient Gly and Mgly concentrations in the

74 atmosphere (Lv et al., 2019). On a global scale, isoprene and ethyne are the most

75 important precursors of Gly and Mgly; on the local scale, however, degradation of

76 aromatics is the major pathway for the production of Gly and Mgly in urban and sub-

77 urban areas. For example, the oxidation of aromatics contributed to approximately 75%

78 of Gly formation in Mexico City (Li et al., 2014; Volkamer et al., 2007).

79   As for the atmospheric sink for Gly and Mgly, photolysis, reaction with OH, dry

80 deposition, and heterogenous processes are considered as the main loss pathways,

81 among which aerosol uptake is most complicated and needs more comprehensive

82 exploration (De Haan et al., 2018; McNeill, 2015; Knote et al., 2014; Fu et al., 2008).

83 The uptake of Gly and Mgly onto inorganic or organic particles has been studied in

84 laboratory experiments under controlled conditions (De Haan et al., 2018; Liggio et al.,

85 2005), and uptake coefficients (γ) were measured by the loss of gas phase concentration

86 or the increase of particle organic mass, within the range of $\sim 10^{-4}$ to 10^{-2} (De Haan et

87 al., 2018; Pye et al., 2017; Liggio et al., 2005). The lower γ value was probably related

88 to the kinetic limitations (Ervens and Volkman 2010), while the higher γ value may be

89 associated with the increased particle acidity (Liggio et al., 2005), relative humidity

90 (De Haan et al., 2018; Corrigan et al., 2008) and ionic strength (Kroll et al., 2005). In

91 addition, ammonium-catalyzed and OH reactions were found to have significant

92 influences on the surface uptake of dicarbonyls (Knote et al., 2014; Kampf et al., 2013;

93 Noziere et al., 2009), and the rate coefficients were found to increase with the increasing

94 ammonium ion activity (a_{NH4+}) and pH (Noziere et al., 2009). The "salting-in" effects

95 resulted from the increased ionic strength could cause significant increase ($\sim$ 3 orders

96 of magnitude) of henry's law constant for Gly, affecting the gas-aqueous partitioning of

97 Gly and enhanced the available Gly for aqueous reactions (Kampf et al., 2013; Knote

98 et al., 2014; Waxman et al., 2015).

99   The uptake processes of Gly and Mgly derived from the laboratory studies were

Atmospheric
Chemistry
and Physics
Discussions
Open Access
EGU

100   incorporated into different models to investigate their formation and destruction (Pye
101   et al., 2017 and references therein; Knote et al., 2014; Li et al., 2014; Ge et al., 2011).
102   It was found that solely incorporating the irreversible uptake pathways of dicarbonyls
103   could lead to high discrepancy between the observation and simulation results from the
104   global 3D model and other models (Hu et al ., 2017; Li X et al., 2014; Li et al., 2013a),
105   highlighting the needs to consider more comprehensive processes including both
106   reversible and irreversible pathways for better simulating the dicarbonyls. Those
107   previous studies showed that the contribution of heterogeneous processes to the
108   destruction of dicarbonyls varied in the range of 0~80%, which depended on the relative
109   humidity, the precursors incorporated into the model as well as the aerosol
110   concentrations for the given region (Knote et al., 2014).

111   The Pearl River Delta (PRD) region has been experiencing rapid industrialization
112   and urbanization in the last three decades, making it one of the most developed regions
113   in China. The filed measurement results suggested that OA contributed 30~40% to
114    $PM_{2.5}$ mass, and SOA dominated the OA with fractions up to ~80% in PRD (Huang et
115   al., 2014; He et al., 2011). Furthermore, the contribution of SOA in $PM_{2.5}$ has been
116   increasing in recent years, highlighting the necessity for better understanding the
117   formation of SOA in this region (Wu et al., 2019; Wang et al., 2019). However, model
118   simulation which provides robust information of the influence of physical processes
119   and chemical degradation in SOA formation still underpredict the SOA abundance with
120   only traditional VOC precursors incorporated, hindering the better understanding the
121   sources and formation mechanism of SOA in PRD (Wu et al., 2019; Fu et al., 2012;
122   Wang et al., 2009). It was found that incorporating emissions of Gly and Mgly, and their
123   degradation mechanisms could effectively narrow the gap between the measured and
124   modelled SOA (Fu et al., 2012; Li et al., 2013a). However, only the simple
125   parameterization of surface uptake of Gly and Mgly without detailed physical and
126   chemical processes (e.g., reversible partitioning of Gly and Mgly into deliquesced
127   droplets) in the model could bias the evolution of Gly and Mgly, leading to the poor
128   understanding on the budgets of Gly and Mgly, their relationship with precursors, and
129   the contributions of precursors to SOA formation in PRD (De Haan et al., 2018;
130   Waxman et al., 2015; Knote et al., 2014; Li et al., 2013a, 2014; Lu et al., 2013).

131   Therefore, to improve the model performance for the simulation of Gly and Mgly and

132   to investigate their evolution and contribution to SOA formation, the observation data

133   from a receptor site in the PRD region was analyzed by a photochemical box model

134   with near-explicit chemical mechanisms (*i.e.,* the master chemical mechanism, MCM),

135   and improvements with reversible and irreversible heterogeneous processes of Gly and

136   Mgly, and the gas-particle partitioning of oxidation products in the present study. The

137   production and evolution of Gly, Mgly, and other intermediate products were

138   investigated. The observed and simulated levels of Gly and Mgly were compared to

139   evaluate the performance of the model, which was further used to quantify the

140   contributions of individual VOCs to SOA formation at the receptor site of PRD.

141

142   **2. Methodology**

143   ***2.1. Field measurement***

144   Field measurements were carried out at Guangdong provincial atmospheric

145   supersite located at Heshan (22.728°N, 112.929°E, 60 m above sea level) in Jiangmen

146   City of the PRD region. The sampling site is located about 50 km and 80 km southwest

147   from Foshan and Guangzhou City, respectively. The Heshan site is surrounded by

148   mountain areas with trees and subtropical plants, and the location of the site is showed

149   in Figure 1. Ambient measurement of VOCs, carbonyls and other trace gases was

150   conducted during January 02- 07, 2017, when the dominant wind was mainly from the

151   southeast where the center of PRD (*i.e.,* Zhuhai and Zhongshan) was located. A detailed

152   description of the Heshan site and the measurement methodology was provided in a

153   previous work (Chang et al., 2019).

154

155

156

157 Figure. 1 The location of sampling site and its surrounding environment in the Pearl River Delta
158 region. The base map was from © Google Maps.

159

160　　　Briefly, mono-carbonyls and Gly and Mgly were collected with 2,4-
161 dinitrophenylhydrazine cartridges every 3 h and detected using a high-performance
162 liquid chromatography (HPLC) system (PerkinElmer 200 Series, US). The hourly
163 VOCs were measured using a cryogen-free automatic gas chromatograph system
164 equipped with a mass spectrometer and a flame ionization detector (GC-MS/FID)
165 (Wang et al., 2014). CO, SO_2, and O_3 was measured using a gas filter correlation
166 analyzer, a pulsed fluorescence analyzer, and a UV photometric analyzer, respectively
167 (Thermo Scientific 48i, 43i, 49i). NO and NO_2 were detected using a
168 chemiluminescence instrument (Thermo Scientific 42i) with a photolytic converter (Xu
169 et al., 2013). The method detection limits for non-methane hydrocarbons (NMHCs),
170 carbonyls, CO, SO_2, O_3, NO, and NO_2 were 20-300, 20-450, 4000, 100, 500, 60, and
171 300 pptv, respectively (Yun et al., 2018; Chang et al., 2019; Li et al., 2020). The
172 measurement method uncertainty of the retrieved Gly and Mgly mixing ratios was
173 estimated around 15% (Chang et al., 2019; Li et al., 2020). Furthermore, hourly
174 meteorological parameters including temperature, wind speed, wind direction, pressure,
175 and relative humidity were recorded using a pyranometer (CMP22, Kipp & Zonen B.V.,
176 Holland) and a portable weather station (Model WXT520, Vaisala, Finland).

177

178 ***2.2. Photochemical box model with master chemical mechanism (PBM-MCM) and***
179 ***gas-particle partitioning SOA scheme***
180　　　Photochemical box model (PBM) was employed in this study to simulate the
181 oxidation of Gly, Mgly and different VOCs, based on a master chemical mechanism

182   (MCM) coupled with a gas-particle partitioning module to represent the SOA formation

183   scheme. The MCM (version 3.2) is a near-explicit mechanism including ~16,500

184   reactions involving ~6,000 chemical species with the latest IUPAC inorganic

185   nomenclature, which described the chemical degradation of ~143 primary VOCs and

186   their oxidation products. The MCM scheme has been applied to different photochemical

187   box models to investigate the oxidation and reactivates of various VOCs, the formation

188   of photochemical O_3 and secondary organic products, atmospheric radical budget and

189   propagation, as well as the policy evaluation on mitigating the photochemical smog

190   (*e.g.,* Ling et al., 2014, 2019; Wang et al., 2017; Lyu et al., 2015; Xue et al., 2014a, b;).

191   The physical processes including dry deposition and atmospheric dilution due to the

192   variations of planetary boundary layer heights (configured according to the local

193   observation in the PRD region from previous studies (Li et al., 2014; Wang et al., 2013;

194   Fan et al., 2011) were considered in the model, but not the influence of horizontal and

195   vertical transport.

196   In addition to the gas-phase degradation of VOCs, a gas-particle partitioning

197   module for the oxidation products of VOCs and those compounds with an estimated

198   normal boiling temperature greater than 450 K, as developed by Johnson et al (2006),

199   were incorporated into the model to represent the SOA formation scheme (Johnson et

200   al., 2005, 2006; Kamens et al., 1999; Stein et al., 1994). In brief, the gas-to-particle

201   equilibrium partitioning of the species was described by the partitioning coefficient (K_p,

202   unit: $m^3 \mu g^{-1}$) using Eq. 1 (Johnson et al., 2006).

$$K_p = \frac{7.501 \times 10^{-9} RT}{MW_{Om} \xi P_L^0}$$

203   (Eq.1)

204   where R, T, MW_{om}, and ξ are the ideal gas constant (8.314 J $K^{-1} mol^{-1}$), temperature (K),

205   the mean molecular weight of the absorbing particle organic matter (g mol^{-1}), and the

206   activity coefficient of species in the condensed organic-phase, respectively. P^o_L is the

207   liquid vapor pressure and was estimated using a semi-empirical expression of the

208   Clausius-Clapeyron equation (Eq. 2):

$$\ln(\tfrac{P_L^0}{760}) = -\frac{\Delta S_{vap}(T_b)}{R}[1.8(\frac{T_b}{T} - 1) - 0.8(\ln(\frac{T_b}{T}))]$$

209   (Eq.2)

210   where T_b was the boiling temperature of different species, which was estimated using a

211   previously described fragmentation method (Stein et al., 1994; Johnson et al., 2006).

212   ΔS_{vap} (T_b) was the vaporization entropy change at T_b, which was estimated using the

Atmospheric
Chemistry
and Physics
Discussions

213   Trouton-Hildebrand-Everett rule with corrections for polar compounds and compounds

214   with hydrogen-bonding capacity (Baum 1997). The concentration of species j in the

215   condensed organic-phase ($F_{j,om}$) can be calculated as the following equation (Eq. 3):

216    $F_{j,om} = M_{om} \times \left(K_{p,j} \times A_j \right)$ (Eq.3)

217   where M_{om} is the total mass concentration of each condensed organic material from gas-

218   particle partitioning, A_j is its gas-phase concentration, and $K_{p,j}$ is its partitioning

219   coefficient of species j (Johnson et al., 2006).

220   The partitioning process was dynamically represented as an equilibrium between

221   absorption and desorption, as described by Kamens et al. (1999). Briefly, the species-

222   dependent K_p values were defined in terms of absorption (k_{in}) and desorption (k_{out}) rate

223   coefficients, with $K_p = k_{in}/k_{out}$. The value for k_{in} ($k_{in} = 6.2 \times 10^{-3}$ m^{3}µg^{-1}s^{-1}) was

224   configured as suggested by Johnson et al. (2006). Thus the K_p could be expressed in

225   terms of k_{out}. More detailed description of the equations and parameters are given by

226   Johnson et al. (2005, 2006) and Kamens et al. (1999).

227

228   *2.3. Partitioning and reactions of gas-phase dicabonyls on particles*

229   The partitioning and reactions of dicarbonyls in the aerosol aqueous phase may

230   involve both irreversible and reversible processes (Ervens and Volkamer, 2010). In the

231   present study, we follow the mechanism proposed by Knote et al. (2014) and consider

232   the reversible partitioning in aqueous phase, the irreversible volume reactions and

233   irreversible surface uptake processes in our model.

234   The reversible partitioning of Gly and Mgly on aerosols aqueous phase is usually

235   described by the Henry's law equilibrium (Kampf et al., 2013) (Eq.4):

236    $[Gly(Mgly)]_{liquid} = K_H \times [Gly(Mgly)]_{gas}$ (Eq.4)

237   However, hydration of carbonyls function groups and salt-Gly interactions could have

238   significant influences on the K_H value of Gly (Kampf et al., 2013; Waxman et al., 2015),

239   and an effective Henry's law coefficient expressed by Eq.5 was often used.

240    $$K_{H,effective} = \frac{K_{H,water}}{10^{(-0.24 \min(12.0,(C_{as}+C_{an}))}}$$ (Eq.5)

241   where the C_{as} and C_{an} represent the concentrations of ammonium sulfate and nitrate.

242   The detailed information on each parameter in these equations have been provided in

243 Kampf et al. (2013), Waxman et al. (2015) and the supplementary of the present study.

244 As variations were found for the value of $K_{H,effective}$ under different concentrations of

245 ammonium sulfate and nitrate in previous studies (Knote et al., 2014; Kampf et al.,

246 2013; Erverns and Volkamer, 2010), the C_{as} and C_{an} were calculated every hour in the

247 present study from the measured ammonium sulfate (and ammonium nitrate)

248 concentrations (mol m^{-3}) divided by aerosol liquid water content (ALWC, kg m^{-3}),

249 which were determined by the aerosol inorganics model (AIM-IV,

250 http://www.aim.env.uea.ac.uk/aim/model4/model4a.php) with inputs of the observed

251 parameters (*e.g.*, ambient relative humidity, temperature, and the moles of each ion) at

252 the Heshan site (Chang et al., 2019).

253   The reversible formation of monomer (*i.e.*, glyoxal, glyoxal monohydrate, and

254 glyoxal dihydrate) and oligomers are considered with the two important reservoirs (*i.e.,*

255 monomer and oligomer pools, represented as pool1 and pool2) (Knote et al. 2014). The

256 variations of the glyoxal monomer ($[Gly_{p1}]$) and oligomer concentrations ($[Gly_{p2}]$) with

257 time can be represented by the following equations (Erverns and Volkamer, 2010;

258 Kampf et al., 2013; Knote et al., 2014):

259
$$\frac{d([Gly_{p1}])}{dt} = \frac{1}{\tau_1} \times (Gly_{p1,eq} - Gly_{p1}) \text{ (Eq.6)}$$

260
$$\frac{d([Gly_{p2}])}{dt} = \frac{1}{\tau_2} \times (Gly_{p2,eq} - Gly_{p2}) \text{ (Eq.7)}$$

261
$$\frac{Gly_{p2,eq}}{Gly_{p1,eq}} = K_{olig} \quad \text{(Eq.8)}$$

262 The equilibrium partitioning between monomers and oligomers was presented as K_{olig}

263 (Eq.8). The definition and configuration of each parameters above were provided in the

264 supplementary according to Knote et al. (2014) and Kampf et al. (2013).

265   In addition, three irreversible pathways of Gly, including 1) the ammonium-

266 catalyzed volume pathway, 2) the OH-reaction volume pathway, and 3) the irreversible

267 surface uptake, were parameterized in the model (Knote et al., 2014; Ervens and

268 Volkman 2010). The ammonium-catalyzed reactions, with rate constant depending on

Atmospheric
Chemistry
and Physics
Discussions

269   both particle acidity (pH) and the activity of the ammonium ion (a_{NH4}), were

270   parameterized as follows when the monomer and oligomer concentrations were in

271   equilibrium (Eq. 9):

272    $K = 2 \times 10^{-10} \times \exp(1.5 \times a_{NH_4}) \times \exp(2.5 \times pH) \times Gly_{p1}$ (Eq.9)

273   This parameterization was configured based on the assumption that only total

274   concentration in the monomer pool was the only particulate glyoxal available to the

275   ammonium-catalyzed reaction as the reversibly formed oligomers do not evaporate

276   easily (Knote et al., 2014; De Haan et al., 2009; Noziere et al., 2008).

277   For OH pathway, the gas-phase OH was in equilibrium with liquid-phase OH by

278   a Henry's law constant ($K_{I,OH}$= 25 M atm^{-1}) with the consideration of the "salting-in"

279   impact (Ervens and Volkamer 2010), and constant of reactions between OH and Gly

280   was 1.1×10^{-9} M^{-1} s^{-1} (Buxton et al., 1997). As suggested by Knote et al. (2014), the Gly

281   concentration available to the OH-reaction pathway was the total glyoxal concentration

282   in the monomer pool.

283   Surface-controlled irreversible uptake of Gly has been widely employed in

284   different modeling studies (Ervens et al., 2011; Li et al., 2014; Liu et al., 2007), was

285   parameterized as follows (Eq.10):

286    $K_r = -\dfrac{\gamma_{gly(mgly)} \times S_{aw} \times \nu_{gly(mgly)} \times C^*_{gly(mgly)}}{4}$ (Eq.10)

287   where $C^*$and ν are the gas-phase concentration and mean molecular velocity,

288   respectively. γ represents the uptake coefficient for Gly and Mgly. Here we use the

289   surface uptake coefficients (γ_{gly}= 1.0×10^{-3} and γ_{Mgly}= 2.6×10^{-4}) to account for the

290   irreversible surface uptake of Gly and Mgly, respectively. It is noted that the surface

291   uptake coefficient of Gly was configured according to the results of uptake kinetics

292   experiments from Schweitzer et al. (1998), which has been used in the model simulation

293   of Gly in the previous PRD study (Li et al., 2014). On the other hand, the surface uptake

294   coefficient of Mgly was obtained via scaling to glyoxal uptake coefficient by the

295   relative Henry's low coefficient suggested by Pye et al. (2017). S_{aw}

296   ($S_{aw}=S_a \times f$(RH)=$S_a \times (1+a \times$(RH)^b)) is the RH corrected aerosol surface area density (Li

297   et al., 2014). The value for a (2.06) was configured as those suggested previously (Liu

298   et al., 2007), while the dry aerosol surface concentration (S_a) was obtained from the

299   measurement at the Heshan site (Yun et al., 2018). In this study, the mean molecular

300   velocities of Gly were calculated by the HyperPhysics model (http://hyperphysics.phy-

301   astr.gsu.edu/hbase, last access date: 06 June 2019). The carbonaceous and insoluble

302   components were considered as an aqueous shell for aerosols, whereas the aerosol

303   surface was fully covered with an aqueous layer (Li et al., 2015).

304   On the other hand, though heterogeneous processes of Mgly are similar to those

305   of Gly, some difference between these two species were found. The Henry's law

306   constant for Mgly is not as effective as that for Gly. Hence, a Henry's law constant (3.7

307     $\times 10^3 \, \text{M atm}^{-1}$) for Mgly we used (Zhou and Mopper 1990). In fact, Kroll et al. (2005)

308   suggested that no aerosol growth was observed from gas-phase Mgly presumably

309   because of its more stable (less electron deficient) ketone moiety, and a recent study

310   indicated that less Mgly would partition into the aerosols than expected according to

311   Henry's law (Waxman et al., 2015). In addition, the surface uptake coefficient ($\gamma_{Mgly} =$

312   2.6×10^{-4}) suggested by Pye et al. (2017) is lower than that extracted from the chamber

313   study (De Haan et al., 2018), which reported the value of γ_{Mgly} could increase to $3.7 \times$

314   10^{-3} at 95% RH and even larger than Gly in a high relative-humidity environment

315   ($\geq$95%). However, they also figured out that treating the surface uptake of Mgly on

316   aerosols as an irreversible pathway could probably overestimate its positive effect for

317   SOA formation via heterogeneous processes, because ~20% of SOA which were

318   formed from Mgly via aqueous processes would further hydrolyze.

319

320   ***2.4. Model scenarios***

321   According to the discussion above, it could be seen that the heterogeneous

322   processes we described for Gly was more complicated than that for Mgly, as the

323   parameterization for the sink of Gly from laboratory and model studies were more

324   robust. Therefore, the present study put more emphasis on the evolution of Gly for

325   better understanding and evaluating the effects of the different sink pathways on

326   dicarbonyls and its influence on SOA formation. Table 1 provides detailed information

327 regarding all the model scenarios for the simulation of Gly, while the model scenarios

328 for Mgly are also given in Table S1 in the supplement.

329 Table 1. Model scenarios used for gas-phase Gly

Scenarios	Description	Purpose
INITIAL	Default MCMv3.2, without considering the reversible and irreversible uptake of Gly and the gas-particle partitioning of other oxidation products	Base run
scenario 1	As INITIAL, also considers ammonium-catalyzed reactions of Gly through monomers pool 1 without the reversible formation of oligomers pool 2.	Investigating the influence of Ammonium reactions on the destruction of Gly
scenario 2	As scenario 1, also considers OH reactions of Gly through monomers pool 1 without the reversible formation of oligomers pool 2.	Investigating the influence of OH reactions for the destruction of Gly
scenario 3	As scenario 2, and considers the aqueous oligomers formation (pool 2) and revisable process with monomers (pool 1).	Investigating the "salting in" impact
scenario 4	As scenario 3, and considers surface uptake by aerosols of Gly with the uptake coefficient of 1×10^{-3} suggested by Li et al. (2014).	Investigating the influence of surface uptake

330

331 In this study, hourly observation data of CO, SO_2, NO, NO_2, O_3, and all measured

332 NMHC and meteorological parameters were used as input and constraints in the model.

333 The photolysis rates, which were not measured, were modified in the model using the

334 photon fluxes from the Tropospheric Ultraviolet and Visible Radiation (TUV-v5) model

335 (Madronich and Flocke 1997) according to the sampling location and modeling period.

336 Model simulation was performed on January 07-08, 2017, when both daily Gly and

337 Mgly data were available, with 00:00 LT (local time) as the initial time. Before the

338 simulation, the model was pre-run for 5 days using the mean diurnal variability of the

339 input species during the whole sampling period to achieve a steady state for the

340 unmeasured species with a short lifetime, *i.e.,* OH and HO_2 radicals (Xue et al., 2014a,

341 b).

342

343 **2.5. Model uncertainty**

344 Uncertainties in the simulation of Gly and Mgly by the model were noted. The total

Atmospheric
Chemistry
and Physics
Discussions

Open Access

EGU

345 model errors could be calculated conservatively from 1) the uncertainties in the

346 measurement of trace gases and NMHCs; 2) the measured data of meteorological

347 parameters, *i.e.,* temperature T, pressure P, and the calculated photolysis frequencies J

348 based on meteorological conditions; 3) reaction rate constants k; and 4) the dry

349 deposition. In this study, following Li et al. (2014) and Lu et al. (2013), the uncertainty

350 factors for the above parameters were adopted as suggested previously (Table S2), and

351 all parameters were divided into three groups (*i.e.,* physical parameters, radical and

352 trace gas concentrations, and reaction rate constants of non-photolytic reactions). Each

353 parameter was multiplied by its uncertainty factor first, and the gaussian error

354 propagation was then applied within each group. We run the model n times (n is the

355 number of parameters considered). The mean diurnal variation of the uncertainty of

356 modeled Gly and Mgly is shown in Figure S1. The total uncertainties of the modelled

357 Gly and Mgly were both estimated to be around 39% with the contributions from radical

358 and trace gas concentrations (~19%), physical parameters (~13%) (included photolysis

359 frequencies, deposition lifetime, T, etc.) and reaction rate constants of non-photolytic

360 reactions (~7%), respectively.

361

362 ***3. Results and Discussion***

363 ***3.1. Comparison between the simulation and observation***

364   The simulated dicarbonyls from the photochemical box model under different

365 scenarios were examined and compared with the observation. The predicted

366 dicarbonyls from in-situ formation in the INITIAL scenario was found to generally

367 overpredict the mixing ratios of Gly and Mgly, and were about 3.3 and 3.5 times of the

368 observed concentrations at the Heshan site, respectively. Similar overestimation has

369 been reported in previous modeling studies, for example, the simulations with only the

370 MCM gas-phases schemes overpredicted the Gly concentration by factors of 2-6 in both

371 urban Mexico City (Volkamer et al., 2007) and a semi-rural site of the PRD region (Li

372 et al., 2014). The significant overestimation in simulation results indicates that there

373 were important loss pathways for Gly and Mgly other than the oxidation reactions (*e.g.,*

374 by OH and NO$_3$ radicals). A sensitivity analysis was firstly conducted with twice the

375 dilution rate (and deposition velocities) in INITIAL scenario, which resulted in the

376 reduction of modeled concentrations of Gly and Mgly by 3.2% (2.8%) and 9.2% (7.9%),

377   respectively (Table S3). Though these enlarged rates were higher than the upper limits

378   of the dilution rate and deposition velocities in previous studies (Fan et al., 2011; Wang

379   et al., 2013; Li et al., 2014), the predicted mixing ratios of Gly and Mgly were still three

380   times higher than the measured levels, suggesting that the dilution and dry deposition

381   configuration could not be the main causes for the overestimation of modeled Gly and

382   Mgly mixing ratios (Volkamer et al., 2006, 2007).
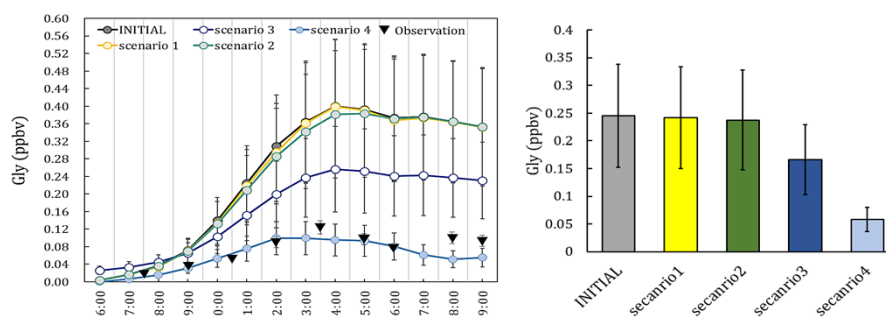
383

384   Figure 2. The observation data, the concentrations and the daily average concentration of Gly
385   predicted from the different scenarios.

386

387   To identify the causes of discrepancy and improve model performance, sensitivity

388   analysis with different heterogenous mechanisms incorporated in the model scheme (as

389   scenarios listed in Table 1) was conducted. The average diurnal patterns of Gly

390   simulated by different model scenarios are showed in Figure 2. It can be seen that in

391   the early morning (*i.e.*, 0600 to 0800 LT, local time), the predicted mixing ratios of Gly

392   in different scenarios were comparable to the observation. In contrast, the difference

393   became larger from 0900 LT onwards, though the predicted peaks of Gly by different

394   model scenarios were all presented at the early afternoon, following by a slow decrease

395   in the late afternoon. The model results from Scenario 4 was more consistent with the

396   observational data. The relative changes of modeled Gly concentrations by adding

397   additional heterogeneous processes to the model scenario INITIAL (*i.e.*, model

398   scenarios 1-4) were summarized in Table S4.

399   On average, by including additional irreversible and reversible pathways, the

400   modeled Gly concentrations during daytime (06:00-19:00) decrease by 72.3% of the

401   values predicted by the INITIAL scenario, and a significant decrease of Gly

402   concentration occurred by adding the effect of surface uptake pathway (*i.e.*, model

403   scenarios 3-4). Similar results have been obtained in a previous study in summer in the

404 PRD region (Li et al., 2014), which found that the simulated Gly concentration decrease

405 significantly (~45 %) in the daytime (*i.e.*, 0600 to 1900 LT) when heterogeneous uptake

406 process was considered with the incorporation of a single uptake coefficient.

407   The contribution of different heterogeneous sink pathways is calculated based on

408 the scenario 4 (Figure S2). The irreversible pathways of Gly (*i.e.*, surface uptake by

409 aerosols, OH and ammonium reactions) accounted for 67.3% of the total sink of Gly,

410 among which the surface uptake was a dominant pathway (61.7%) comparing to the

411 ammonium and OH reactions (2.5% and 2.9%, respectively). The reversible pathway

412 made a relatively lower contribution to the total sink of Gly (32.9%).

413   In addition, the heterogeneous irreversibly and reversibly pathways of Mgly was

414 also investigated in the sensitivity analysis (*i.e.*, model scenarios M1-2, listed in Table

415 S5), and the predicted Mgly concentrations during daytime (0600-1900 LT) decreased

416 by 73.0% of the values estimated in INITIAL model scenario. The surface uptake

417 pathway in the scenario M2 was found to be the most important heterogeneous pathway

418 for the loss of Mgly, and contributed to 64.1% of the total sink of Mgly. The

419 contributions of the reversible pathway to the destruction of Mgly was around 35.9%

420 (Figure S3).

421   Overall, by incorporating a more detailed heterogeneous processes of Gly and

422 Mgly, the results of scenarios 4 and M2 provided better agreement between the modeled

423 and measured Gly and Mgly. The results demonstrated the significance of

424 heterogeneous uptake processes on the destruction of Gly and Mgly, and adopting the

425 irreversible/reversible pathways (*i.e.*, the reversible partitioning, volume reactions, and

426 the surface uptake) could reasonably reproduce the variations of Gly and Mgly at the

427 Heshan site in the PRD region.

428

429 ***3.2. Process analysis on the production and destruction of Gly and Mgly***

430   The scenario 4 simulation with the best agreement with measurement was further

431 analyzed to investigate the photochemical budget of Gly and Mgly at the Heshan site,

432 respectively (Table 2). It was found that OH oxidation of aromatics was the most

433 important contributor for the Gly and Mgly production, with mean contributions of ~80%

434 and ~94%, respectively. Among all the aromatic precursors, toluene and *m,p*-xylene

435 were the two major precursors for the formation of Gly and Mgly, with total

436 contributions of ~43% and ~56% of Gly and Mgly formation, respectively. In contrast,

Atmospheric
Chemistry
and Physics
Discussions

Open Access

EGU

437 because of the relatively low photochemical reactivity, benzene and alkanes had lower

438 contributions on the formation of Gly and Mgly in the present study, although they can

439 travel a long distance and contribute to secondary Gly and Mgly in areas far from their

440 emissions (Lv et al., 2019). Different from previous studies that found the isoprene as

441 the key precusors for Gly and Mgly formation (Li et al., 2014; Lou et al., 2010), the

442 contributions of isoprene oxidation at the Heshan site in the present study were much

443 lower than that of aromatics, with only mean contributions of ~2% and ~3%,

444 respectively. It can be attributed to the lower mixing ratios of isoprene (*i.e.,* 70 ± 10

445 pptv) observed at Heshan site because of the lower temperature in winter, comparing to

446 the much higher concentration observed during summer (average of ~1ppb and

447 maximum of ~ 4 ppbv in the afternoon) in the rural and forest areas in this region (Li

448 et al., 2014; Lou et al., 2010).

449   In addition, the relative contributions of different loss pathways of Gly and Mgly,

450 including physical processes (vertical dilution and dry deposition), and the

451 heterogeneous processes of Gly and Mgly on aerosols were also estimated from the

452 PBM-MCM model results (Table 2). Consistent with previous studies (Atkinson and

453 Arey, 2003; Ervens et al., 2011), heterogeneous processes were the most important

454 pathway for the destruction of Gly and Mgly (both with contributions of ~62%),

455 followed by photolysis (with contributions of ~26% and ~25%, respectively).

456

457   Table 2 Production and destruction of Gly and Mgly from model simulation

Precursor	Oxidant	Gly		Mgly	
		Molar yield (%)[a]	Contribution (%)	Molar yield (%)[a]	Contribution(%)
Aromatics					
benzene, %	OH	32	4.94	-	-
toluene, %	OH	30.6	23.41	21.5	23.80
m, p-xylene, %	OH	25.2	19.22	35.1	32.08
o-xylene, %	OH	12.7	15.04	33.1	14.49
1,2,4-trimethylbenzene, %	OH	7.2	1.40	27.2	5.98
1,2,3-trimethylbenzene, %	OH	7.8	1.43	15.1	4.54

1,3,5-trimethylbenzene, %	OH	- [c]	-	58.1	13.21
ethylbenzene, %	OH	55	6.62	-	-
p-ethyltoluene, %	OH	31.9	5.45	-	-
m-ethyltoluene, %	OH	7.9	1.52	-	-
o-ethyltoluene, %	OH	8	0.51	-	-
Sum			79.54		94.10
Alkanes					
propane, %	OH	-	-	11	0.73
> C3 alkanes [b],%	OH	1	0.19	3.2	0.71
Sum			0.19		1.44
Alkenes					
	OH	6.2	0.43	25	0.57
isoprene,%	NO_3	43.7	1.34	37.8	2.83
	O_3	4	0.20	-	-
ethene,%	OH	5.7	1.08	-	-
	O_3	0.44	1.15	-	-
> C2 alkenes [b],%	OH	-	-	7.7	1.06
propene, %	O_3	8.3	1.01	-	-
1-pentene, %	O_3	2	0.73	-	-
Sum			5.94		4.46
Acetylene	OH	63.5	14.33	-	-
Loss pathyways					
photolysis, %			26.2		25.1
NO_3,OH-reaction, %			4.06		7.87
dry deposition, %			2.23		1.73
dilution, %			5.71		3.30
heterogeneous [d], %					
Irreversible processes, %			41.0		39.8
Reversible processes, %			20.8		22.2

458 [a] Molar yields were taken from previous studies (Fu et al., 2008) (Fick et al., 2003) (Nishino
459   et al., 2010) (Calvert 2000; Volkamer et al., 2006).
460 [b] >2 alkenes (include 3 alkenes) and >3 alkanes (include 17 alkanes) are represented in this
461   study as a single lumped species (Lv et al., 2019).
462 [c] "−" not applicable.
463 [d] Considered both irreversible and reversible parameterizations of the aerosol sinks (*i.e.*,
464   scenario 4 and **M2**).
465
466 ***3.3 Implications for secondary organic aerosol formation***

467   By incorporating both the traditional gas-particle partitioning (of VOC oxidation

468   products other than Gly and Mgly) and the heterogeneous processes (of Gly and Mgly)

469   into the model, we investigated the contributions of different mechanism in SOA

470   formation through sensitivity analysis. The contributions of VOC oxidations to SOA

471   formed from gas-particle partitioning (SOA$_{gp}$) and SOA formed from heterogeneous

472   processes of Gly and Mgly (SOA$_{het}$) were quantified.

473   On the other hand, based on the SOA$_{gp}$ formation scheme (in scenario 4), the

474   relative importance of each VOC precursor in SOA$_{gp}$ formation was further evaluated

475   to provide a complete picture for SOA$_{gp}$ formation and its relationship with precursors.

476   As with O$_3$ formation, the roles of individual VOC precursors in SOA$_{gp}$ formation were

477   calculated using relative increment reactivity (RIR_{SOAgp}) method, which have been

478   widely used to present the percentage change in the production of secondary products

479   per percent change in precursors. The RIR_{SOAgp} of a specific precursor X at site Z is

480   given by Eq. 11:

481    $RIR_{SOA_{gp}}^{Z}(X) = \dfrac{[P_{SOA_{gp}}^{Z}(X) - P_{SOA_{gp}}^{Z}(X - \Delta X)]/P_{SOA_{gp}}^{Z}(X)}{\Delta Z(X)/Z(X)}$ (Eq.11)

482   where $Z(X)$ represents the measured concentration of precursor X, including the

483   amounts emitted at the site and those transported to the site, and ΔX is the change in the

484   concentration of precursor X caused by a hypothetical change $\Delta Z(X)$ (10% $Z(X)$ in this

485   study). Here, $P_{SOA_{gp}}^{Z}(X)$ represents the SOA$_{gp}$ formation potential. A large positive

486   RIR_{SOAgp} value of a specific precursor suggests that SOA$_{gp}$ formation could be

487   significantly decreased if the emissions of this precursor were controlled. Figure 3

488   depicts the top 10 VOC precursors with high RIR_{SOAgp} values at Heshan site. Both *m,p*-

489   xylene and *o*-xylene had the highest RIR_{SOAgp} value (~0.35), followed by toluene (~0.2)

490   and ethylbenzene (~0.06). As *m/p*-xylene, *o*-xylene and toluene can also have a

491   significant impact on dicabonyls production, they are likely to make a noticeable

492   contribution to both SOA$_{gp}$ and SOA$_{het}$ formation.

493
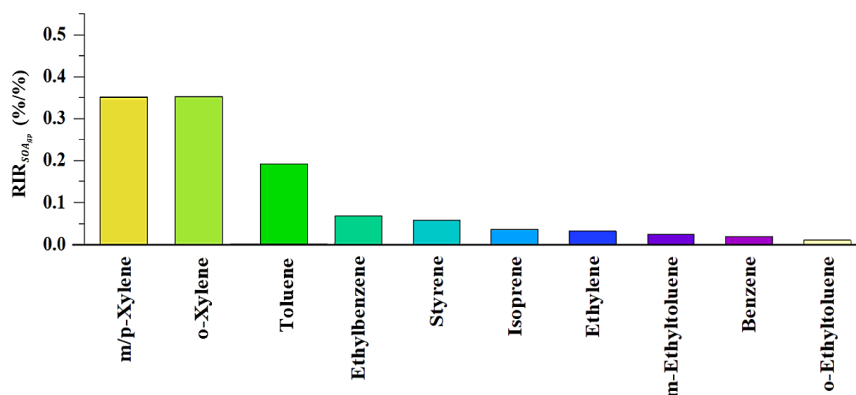
Figure 3. Top 10 VOC precursors with high RIR_{SOAgp} values at Heshan site.

The average diurnal variations of SOA_{het} concentration formed from Gly and Mgly were showed in Figure 4. Both SOA_{het} (Gly) and SOA_{het} (Mgly) concentrations presented photochemistry-driven diurnal patterns, and started to increase in the morning before reaching the maximum value (0.52 and 0.42 μg/m^3) at 1400 and 1200 LT, respectively. It is consistent with the diurnal pattern of SOA_{gp}, which could be formed from the oxidation of other VOCs due to the high photochemical reactivity at noon, which further converted to SOA_{gp} through gas-particle partitioning.-In general, SOA_{gp} made a higher contribution to total SOA (78.6%) than SOA_{het} (21.4%). Previous studies have indicated that the more abundant anthropogenic precursors than biogenic ones under NO$_x$ saturated environment could lead to greater contribution of SOA_{gp} to total SOA despite that the oxidation of anthropogenic species (*i.e.*, aromatics) could lead to relatively higher yields of Gly and Mgly (Knote et al., 2014; Ervens et al., 2011). Ervens et al. (2011) has found that in areas with high concentrations of biogenic precursors at high relative humidity, the SOA_{het} and SOA_{gp} were equally important for total SOA, while in the anthropogenic dominated areas, the contribution of SOA_{het} to the total predicted SOA mass was around 30%. Similarly, the formation of SOA_{gp} and SOA_{het} were both dominated by xylenes and toluene, contributing to ~74%, ~62% and ~69% of SOA_{gp}, SOA_{het} (Gly) and SOA_{het} (Mgly), respectively. Furthermore, *o*-xylene was the most important precursor to the SOA_{gp} (~29%), but only contributed ~16% and ~13% to SOA_{het} (Gly) and SOA_{het} (Mgly) formation, respectively. The toluene and *m,p*-xylene made the most significant contributions to the SOA_{het} (Gly) (26.0%) and SOA_{het} (Mgly) (32.2%) formation, consistent with the chamber results from the oxidations of

Atmospheric
Chemistry
and Physics
Discussions

Open Access

EGU

519   different precursors (Ervens et al., 2011).
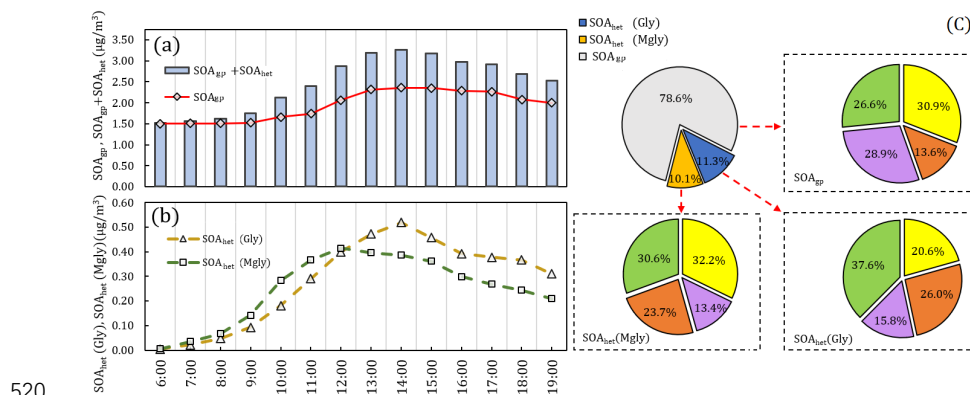
520

521   Figure 4. The average diurnal variations of SOA_{gp}, SOA_{het} (Gly) (*i.e.*, SOA_{het} formed from
522   Gly), SOA_{het} (Mgly) (*i.e.*, SOA_{het} formed from Mgly) and total SOA formation were showed
523   in Figure 4a and 4b. The proportion of SOA_{gp}, SOA_{het} (Gly) and SOA_{het} (Mgly) in total SOA
524   as well as the contribution of VOCs precursors to SOA_{gp}, SOA_{het} (Gly) and SOA_{het} (Mgly)
525   formation, were represented in the pie charts in Figure 4c.
526

3.4 Comparison with previous studies in PRD

528   Previous studies have been conducted to investigate the evolution of Gly and/or

529   Mgly using observation and model simulation in the PRD region. However, one must

530   bear in mind that the mechanisms of the formation and evolution of Gly and/or Mgly

531   were more detailed in the present study, as previous studies in PRD only incorporated

532   the irreversible surface uptake process with a single coefficient for the heterogeneous

533   pathway for dicarbonyls. This may not reflect the current knowledge for the formation

534   and evolution of Gly and/or Mgly and their influence on SOA formation (Knote et al.,

535   2014; Waxman et al., 2015; Sumner et al., 2014).

536   Li et al. (2013a) used the regional air quality model CMAQ to investigate the

537   contributions of the aerosol surface uptake of Gly and Mgly to SOA formation in the

538   PRD region, and an uptake coefficient of 2.9×10^{-3} was used for both Gly and Mgly in

539   the model. Interestingly, the results from their model were about 30% higher than that

540   in our study (Table S6). For example, Li et al. (2013a) concluded that SOA formed from

541   dicabonyls may contribute higher than 50% to the total SOA mass in the PRD region,

542   while our study showed that the contribution of SOA_{het} to total SOA mass was ~21%

543   (*i.e.*, ~11% of SOA_{het} formed from Gly; ~10% of SOA_{het} formed from Mgly). In

544   addition, the averaged concentration of SOA_{het} from Gly (0.28 ug/m^3) and Mgly (0.25

545   ug/m^3) in our study is one order of magnitude lower than that in Li et al. (2013a) (*i.e.*,

546   2.33 and 2.51 ug/m^3, respectively). The discrepancy was mainly due to the different

547   parameterizations of heterogeneous processes of dicabonyls. The parameterization in

548   the Li et al. (2013a) and other previous studies did not consider the reversible processes

549   of dicarbonyls, but used one constant surface uptake coefficient to represent all the

550   heterogeneous processes, which could result in bias in SOA formation if there are

551   available aerosol surfaces without considering the influence of aerosols composition

552   and phase state. Moreover, most of the previous studies using higher surface uptake

553   coefficients intended to narrow the discrepancy between observed and simulated SOA

554   mass without direct comparison between observed and simulated concentrations of

555   dicarbonyls (i.e., Li et al., 2013a; Waxman et al., 2013; Fu et al., 2008; Vokalmer et al.,

556   2007). For example, Knote et al. (2014) conducted a total of seven simulations to

557   investigate the SOA formation from Gly over California. Their results showed that the

558   SOA concentration in SIMPLE scenario (characterized by a single uptake coefficient

559   of 3.3×10^{-3}) was an order of magnitude higher than that in HYBRID scenario

560   (characterized by an uptake coefficient of 1.0×10^{-3} and also considered more

561   comprehensive parameterization of heterogeneous processes). In fact, if we only

562   consider the surface uptake by aerosols for dicabonyls using the same uptake coefficient

563   for dicabonyls (2.9×10^{-3}) as Li et al., (2013a), the contribution of SOA_{het} to total SOA

564   mass would increase to 72% (i.e., 37% of SOA_{het} formed from Gly; 35% of SOA_{het}

565   formed from Mgly) (Table S6). However, this configuration may not reflect the real

566   evolution of dicabonyls, resulting in the underestimation on the dicabonyls

567   concentrations (i.e., the simulated concentration is at least one order of magnitude lower

568   than the observation) (Figure S4) and overprediction of the contribution of SOA_{het} to

569   total SOA mass in this study (~51%).

570   Table 3 compares the surface uptake coefficient derived from laboratory

571   experiments and those used in different model simulation. It could be found that there

572   was a large variation range for the surface uptake coefficients of Gly, while the studies

573   on Mgly were still limited. For example, the laboratory experiment reported the surface

574   uptake coefficients of Gly in the range of (0.8-6.6) and ($\leq 1 - 9$) $\times 10^{-3}$ on aqueous

575   inorganic aerosols and cloud droplet/ice crystals, respectively (Volkamer et al., 2007;

576   Loggio et al., 2005), and the coefficients were found to be $> 2.3 \times 10^{-3}$ for particles

577   with high acidity (pH values within the range of -0.44 to -1.3) (Loggio et al., 2005). On

578   the other hand, Schweitzer et al. (1998) reported that the uptake coefficient of > 0.001

579   was only observed for lower temperature conditions, and the experimentally measured

580   coefficient ranged from $(1.2 \pm 0.06) \times 10^{-2}$ to $(2.5 \pm 0.01) \times 10^{-3}$ on acidic solution (*i.e.*,

581   60-93 wt% H_2SO_4) at 253-273 k (Gomez et al., 2015; Zhang et al., 2015). It is suggested

582   that more accurate and comprehensive parameterization of heterogeneous processes of

583   dicabonyls still needs deeper exploration for further model development. The

584   parameterization used in this study were mostly adopted from previous results, though

585   it may still have limitations and uncertainties, the results of simulation at this site show

586   better agreement with the observation.

587

588   Table 3 Surface uptake coefficient of Gly from laboratory experiments and used in the
589   model simulation in the present and previous studies

Coefficient	References
$(0.8-7.3) \times 10^{-3}$, on aqueous inorganic aerosols	Volkamer et al., 2007; Loggio et al., 2005;
$(\leq 1 - 9) \times 10^{-3}$, and on cloud droplet/ice crystals	Volkamer et al., 2007; Loggio et al., 2005;
$(1.2 \pm 0.06) \times 10^{-2}$ - $(2.5 \pm 0.01) \times 10^{-3}$ on acidic solutions (*i.e.*, 60-93 wt% H_2SO_4 at 253-273 k)	Gomez et al., 2015; Zhang et al., 2015
3.3×10^{-3}	Knote et al., 2014 and references therein; Waxman et al., 2013; Waxman et al., 2013
2.9×10^{-3}	Fu et al., 2008
1.0×10^{-3}	Knote et al., 2014 and references therein; this study; Li et al., 2014

590

591   ### *4. Conclusion*

592   A photochemical box model coupled with MCM (v3.2) (PBM-MCM) and further

593   improvements on the evolution of semi- and non-volatility oxidation products to a

594   condensed particle-phase, was used to investigate the production and heterogeneous

595   processes of Gly and Mgly, as well as the SOA-precursor relationship at a receptor site

596   (*i.e.,* the Heshan site) for the first time in the PRD region. Compared to the

597   measurements, the initial model configuration overestimated the Gly and Mgly

598   concentrations by a factor of 3.3 and 3.5, respectively. This discrepancy occurred

599   largely due to the absence of irreversible uptake and reversible partitioning. Model

600   investigation regarding the production of Gly and Mgly revealed that the oxidation of

601   aromatics by OH radicals was the most important contributor to the formation of Gly

602   and Mgly, with mean contributions of ~80% and ~94%, respectively, with toluene and

603   *m,p*-xylene acting as the most important precursors for Gly and Mgly. For SOA

604   formation, the heterogeneous processes of Gly and Mgly probably can explain ~21%

605   of SOA mass in PRD. Toluene and *m,p*-xylene were the main precursors for SOA_{het}

606   formation, while *o*-xylene was the most important precursor of SOA_{gp}. Moreover,

607   Overall, this study evaluated the formation and heterogeneous processes of Gly and

608   Mgly in a polluted subtropical environment and highlighted the important role of

609   intermediate products that are produced from photochemical oxidation of VOCs in SOA

610   formation. The results of this study are expected to provide a better understanding of

611   the evolution of VOC precursors, intermediate products, and heterogeneous process of

612   the dicarbonyls, and the developed model modules can provide a robust tool for

613   investigating SOA formation in the PRD and other regions in China.

614

642 Special Fund Project for Science and Technology Innovation Strategy of Guangdong
643 Province (Grant No.2019B121205004).

644

References

646 Baum, E., 1997. Chemical property estimation: theory and application. Crc Press.
647 Benavent, N., Garcia-Nieto, D., Wang, S.S., Saiz-Lopez, A., 2019. Max-DOAS
648   measurements and vertical profiles of glyoxal and formaldehyde in Madrid,
649   Spain. Atmos. Environ. 199, 357-367.
650 Buxton, GeorgeáV, Malone, TreenaáN, áArthur Salmon, G. 1997. Oxidation of glyoxal
651   initiated by OH in oxygenated aqueous solution. Journal of the Chemical
652   Society, Faraday Transactions. 9316, 2889-2891.
653 Calvert, G., 2000. Evidence from functional magnetic resonance imaging of crossmodal
654   binding in the human heteromodal cortex. Curr. Biol. 10(11), 649-657.
655 Carlton, A. G., Wiedinmyer, C., Kroll, J. H., 2009. A review of Secondary Organic
656   Aerosol (SOA) formation from isoprene. Atmos. Chem. Phys. 9(14), 4987-5005.
657 Chang, D., Wang, Z., Guo, J., Li, T., Liang, Y. H., Kang, L. Y., Xia, M., Wang, Y., Yu,
658   C., Yun, H., Yue, D. L., Wang, T., 2019. Characterization of organic aerosols
659   and their precursors in southern China during a severe haze episode in January
660   2017. Sci. Total Environ. 691, 101-111.
661 Corrigan, A. L., Hanley, S. W., De Haan, D. O., 2008. Uptake of glyoxal by organic and
662   inorganic aerosol. Environ. Sci. Technol., 42, 4428−4433.
663 De Haan, D. O., Jimenez, N. G., De Loera, A., Cazaunau, M., Gratien, A., Pangui, E.,
664   2018. Methylglyoxal Uptake Coefficients on Aqueous Aerosol Surfaces. J. Phys.
665   Chem. A. 12221, 4854-4860.
666 De Haan, D.O., Corrigan, A.L., Tolbert, M.A., Jimenez, J.L., Wood, S.E., Turley, J.J.,
667   2009. Secondary organic aerosol formation by sel-reactions of methylglyoxal
668   and glyoxal in evaporating droplets. Environ. Sci. Technol. 43, 8184-8190.
669 Digangi, J.P. Henry, S.B., Kammrath, A., Boyle, E.S., Kaser, L., Schnizhofer, R., Graus,
670   M., Turnipseed, A., Park, J-H., Weber, R.J., Hornbrook, R.S., Cantrell, C.A.,
671   Maudlin III, R.L., Kim, S., Nakashima, Y., Wolfe, G.M., Kajii, Y., Apel, E.C.,
672   Goldstein, A.H., Guenther, A., Karl, T., Hansel, A., Keutsch, F.N., 2012.
673   Observations of glyoxal and formaldehyde as metrics for the anthropogenic
674   impact on rural photochemistry. Atmos. Chem. Phys. 12, 9529-9543.
675 Ding, X., He, Q. F., Shen, R. Q., Yu, Q. Q., Wang, X. M., 2015. Spatial distributions of
676   secondary organic aerosols from isoprene, monoterpenes,\r β\r -caryophyllene,
677   and aromatics over China during summer. J. Geophys. Res. Atmos. 119(20),
678   11,877-11,891.
679 Ervens, B. and Volkamer, R., 2010. Glyoxal processing by aerosol multiphase
680   chemistry: towards a kinetic modeling framework of secondary organic aerosol
681   formation in aqueous particles. Atmospheric Chemistry and Physics. 1017,
682   8219-8244.
683 Ervens, B., Turpin, B. J., Weber, R. J., 2011. Secondary organic aerosol formation in
684   cloud droplets and aqueous particles (aqSOA): a review of laboratory, field and
685   model studies. Atmos. Chem. Phys. 1121, 22301-22383.
686 Fan, S. J., Fan, Q., Yu, W., Luo, X. Y., Wang, B. M., Song, L. L., Leong, K. L., 2011.

Atmospheric boundary layer characteristics over the Pearl River Delta, China during summer 2006: measurement and model results. Atmos. Chem. Phys. 1113, 6297-6310.

Fick, J., Pommer, L., Nilsson, C., Andersson, B., 2003. Effect of OH radicals, relative humidity, and time on the composition of the products formed in the ozonolysis of α-pinene. Atmos. Environ. 3729, 4087-4096.

Fu, T.-M., Jacob, D.J., Wittrock, F., Burrows, J.P., Henze, D.K., 2008. Global budgets of atmospheric glyoxal and methylglyoxal, and implications for formation of secondary organic aerosols. J. Geophys. Res. Atmos. 113(D15),

Fu, T.-M., Cao, J.J., Zhang, X.Y., Lee, S.C., Zhang, Q., Han, Y.M., Qu, W.J., Han, Z., Zhang, R., Wang, Y.X., Chen, D., Henze, D.K., 2012. Carbonaceous aerosols in China: top-down constraints on primary sources and estimation of secondary contribution. Atmos. Chem. Phys. 12, 2725-2746.

Ge, Yu, Bayer, Amanda R, Galloway, Melissa M, Korshavn, Kyle J, Fry, Charles G, Keutsch, Frank N. 2011. Glyoxal in aqueous ammonium sulfate solutions: products, kinetics and hydration effects. Environ. Sci. Technol. 4515, 6336-6342.

Gomez, M.E., Lin, Y., Guo, S., Zhang, R., 2015. Heterogeneous chemistry of glyoxal on acidic solutions. An oligomerization pathway for secondary organic aerosol formation. J. Phys. Chem. A. 119, 19, 4457-4463.

Grosjean, D, Grosjean, E, Gertler, A., 2001. On-road emissions of carbonyls from light-duty and heavy-duty vehicles. Environ. Sci. Technol. 351, 45-53.

Guo, S., Hu, M., Guo, Q., Zhang, X., Zheng, M., Zheng, J., Chang, C. C., Schauer, J. J., Zhang, R., 2012. Primary sources and secondary formation of organic aerosols in Beijing, China. Environ. Sci. Technol. 4618, 9846-9853.

He, L-Y., Huang, X.-F., Xue, L., Hu, M., Zheng, J., Zhang, R.Y., Zhang, Y.H., 2011. Submicron aerosol analysis and organic source apportionment in an urban atmosphere in Pearl River Delta of China using high-resolution aerosol mass spectrometry. J. Geophys. Res. 116, D12304, dio:10.1029/2010JD014566.

Hoyle, C. R., Myhre, G., Berntsen, T. K., Isaksen, I. S. A., 2009. Anthropogenic influence on SOA and the resulting radiative forcing. Atmos. Chem. Phys. 9(8), 2715-2728.

Huang, R.J., Zhang, Y.L., Bozzetti, C., Ho, K.F., Cao, J.J., et al., 2014. High secondary aerosol contribution to particulate pollution during haze events in China. Nature 514, 218-222.

Hu, J., Wang, P., Ying, Q., Zhang, H., Chen, J., Ge, X., Li, X., Jiang, J., Wang, S., Zhang, J. and Zhao, Y., 2017. Modeling biogenic and anthropogenic secondary organic aerosol in China. Atmos. Chem. Phy. 17(1), pp.77-92.

Jimenez, J. L., Canagaratna, M. R., Donahue, N. M., Prevot, A. S., Zhang, Q., Kroll, J. H., Decarlo, P. F., Allan, J. D., Coe, H., Ng, N. L., 2009. Evolution of organic aerosols in the atmosphere. Science (New York, N.Y.). 326(5959), 1525-1529.

Johnson, D., Jenkin, M. E., Wirtz, K., Martin-Reviejo, M., 2005. Simulating the formation of secondary organic aerosol from the photooxidation of aromatic hydrocarbons. Environ. Chem. 2(1), 35-48.

731 Johnson, D., Utembe, S. R., Jenkin, M. E., 2006. Simulating the detailed chemical
732   composition of secondary organic aerosol formed on a regional scale during the
733   TORCH 2003 campaign in the southern UK. Atmos. Chem. Phys. 6(2), 419-
734   431.
735 Kamens, R., Jang, M., Chien, C. J., Leach, K., 1999. Aerosol Formation from the
736   Reaction of α-Pinene and Ozone Using a Gas-Phase Kinetics-Aerosol
737   Partitioning Model. Environ. Sci. Technol. 33(9), 1430-1438.
738 Kampf, C. J. , Waxman, E. M. , Slowik, J. G. , Dommen, J. , Pfaffenberger, L. , Praplan,
739   A. P. , André SH, Baltensperger, U, Hoffmann, T, Volkamer, R., 2013. Effective
740   Henry's law partitioning and the salting constant of glyoxal in aerosols
741   containing sulfate. Environ. Sci. Technol. 47(9), 4236-4244.
742 Knote, C., Hodzic, A., Jimenez, JL, Volkamer, R., Orlando, JJ, Baidar, S, Brioude, J,
743   Fast, J, Gentner, DR, Goldstein, AH. 2014. Simulation of semi-explicit
744   mechanisms of SOA formation from glyoxal in aerosol in a 3-D model. Atmos.
745   Chem. Phys. 1412, 6213-6239.
746 Kurtén, T., Elm, J., Prisle, N.L., Mikkelsen, K.V., Kampf, C.J., Waxman, E.M.
747   Volkamer, R., 2014. Computational study of the effect of glyoxal–sulfate
748   clustering on the Henry's law coefficient of glyoxal. J. Geophys. Res. Atmos.
749   119(19), 4509-4514.
750 Kroll, J. H., Ng, N. L., Murphy, S. M., Flagan, R. C., Seinfeld, J. H., 2005. Secondary
751   organic aerosol formation from isoprene photooxidation under high-NOx
752   conditions. Geophys. Res. Lett. 32(18).
753 Li, J., Cleveland, M., Ziemba, L. D., Griffin, R. J., Barsanti, K. C., Pankow, J. F., 2015.
754   Modeling regional secondary organic aerosol using the Master Chemical
755   Mechanism. Atmos. Environ. 102, 52-61.
756 Li, N., Fu, T. M., Cao, JJ., Lee, S., Huang, X. F., He, L. Y., Ho, K. F., Fu, J. S., Lam, Y.
757   F,. 2013a. Sources of secondary organic aerosols in the Pearl River Delta region
758   in fall: Contributions from the aqueous reactive uptake of dicarbonyls. Atmos.
759   Environ. 763, 200-207.
760 Li, X., Brauers, T., Hofzumahaus, A., Lu, K., Li, Y. P., Shao, M., Wagner, T., Wahner,
761   A., 2013b. MAX-DOAS measurements of NO2, HCHO and CHOCHO at a
762   rural site in Southern China. Atmos. Chem. Phys. 13(4), 2133-2151.
763 Li, X., Rohrer, F., Brauers, T., Hofzumahaus, A., Wahner, A., 2014. Modeling of HCHO
764   and CHOCHO at a semi-rural site in southern China during the PRIDE-
765   PRD2006 campaign. Atmos. Chem. Phys. 14, 33013-33054.
766 Li, T., Wang, Z., Wang, Y.R., Wu, C., Liang, Y.H., Xia, M., Yu, C., Yun, H., Wang, W.H.,
767   Wang, Y., Guo, J., Herrmann, H., Wang, T., 2020. Chemical characteristics of
768   cloud water and impacts on aerosol properties at a subtropical mountain site in
769   Hong Kong SAR. Atmos. Chem. Phys. 20, 391-407.
770 Li, Yang, Shao, Min, Lu, Sihua, Chang, Chih-Chung, Dasgupta, Purnendu K. 2010.
771   Variations and sources of ambient formaldehyde for the 2008 Beijing Olympic
772   games. Atmospheric Environment. 4421-22, 2632-2639.
773 Liggio, J., Li, S. M., Mclaren, R., 2005. Reactive uptake of glyoxal by particulate matter.
774   J. Geophys. Res. Atmos. 110(D10).

775 Ling, Z. H., Guo, H., Lam, S. H. M., Saunders, S. M., Wang, T., 2014. Atmospheric
776   photochemical reactivity and ozone production at two sites in Hong Kong:
777   Application of a master chemical mechanism–photochemical box model. J.
778   Geophys. Res. Atmos. 119(17), 10567-10582.

779 Ling, Z. H., He, Z. R., Wang, Z., Shao, M., Wang, X. M., 2019. Sources of methacrolein
780   and methyl vinyl ketone and their contributions to methylglyoxal and
781   formaldehyde at a receptor site in Pearl River Delta. J. Environ. Sci. 5, 1-10.

782 Liu, Y., Shao, M., Lu, S., Chang, C. C., Wang, J. L., Chen, G., 2007. Volatile Organic
783   Compound (VOC) measurements in the Pearl River Delta (PRD) region, China.
784   Atmos. Chem. Phys. 7(5), 1531-1545.

785 Lou, S., Holland, F., Rohrer, F., Lu, K., Bohn, B., Brauers, T., Chang, C. C., Fuchs, H.,
786   Häseler, R., Kita, K., Kondo, Y., Li, X., Shao, M., Zeng, L., Wahner, A., Zhang,
787   Y., Wang, W., Hofzumahaus, A., 2010. Atmospheric OH reactivities in the Pearl
788   River Delta – China in summer 2006: measurement and model results. Atmos.
789   Chem. Phys. 1022, 11243-11260.

790 Lu, K. D., Hofzumahaus, A., Holland, F., Bohn, B., Brauers, T., Fuchs, H., Hu, M.,
791   Häseler, R., Kita, K., Kondo, Y., Li, X., Lou, S. R., Oebel, A., Shao, M., Zeng,
792   L. M., Wahner, A., Zhu, T., Zhang, Y. H., Rohrer, F., 2013. Missing OH source
793   in a suburban environment near Beijing: observed and modelled OH and HO2
794   concentrations in summer 2006. Atmos. Chem. Phys. 13(2), 1057-1080.

795 Lv, S., Gong, D., Ding, Y., Lin, Y., Wang, H., Ding, H., 2019. Elevated levels of glyoxal
796   and methylglyoxal at a remote mountain site in southern China: Prompt in-situ
797   formation combined with strong regional transport. Sci. Total Environ. 672,
798   869-882.

799 Lyu, X. P., Chen, N., Guo, H., Zhang, W. H., Liu, M., 2015. Ambient volatile organic
800   compounds and their effect on ozone production in Wuhan, central China. Sci.
801   Total Environ. 541(60), 200-209.

802 Madronich, S., Flocke, S., 1997. Theoretical estimation of biologically effective UV
803   radiation at the Earth's surface. Solar ultraviolet radiation.

804 McNeill, V. F. 2015. Aqueous Organic Chemistry in the Atmosphere: Sources and
805   Chemical Processing of Organic Aerosols, Environ. Sci. Technol., 49, 1237–
806   1244.

807 Nishino, N., Arey, J., Atkinson, R., 2010. Formation yields of glyoxal and
808   methylglyoxal from the gas-phase OH radical-initiated reactions of toluene,
809   xylenes, and trimethylbenzenes as a function of NO_2 concentration. J. Phys.
810   Chem. A. 114(37), 10140-10147.

811 Noziere, B., Dziedzic, P., Córdova, A., 2008. Products and kinetics of the liquid-phase
812   reaction of glyoxal catalyzed by ammonium ions (NH_4^+). J. Phys. Chem. A.
813   113(1), 231-237.

814 Pye, H. O. T., Murphy, B. N., Xu, L. , Ng, N. L., Carlton, A. G., Guo, H., 2017. On the
815   implications of aerosol liquid water and phase separation for organic aerosol
816   mass. Atmos. Chem. Phys. 17(1), 343-369.

817 Schweitzer, F., Magi, L., Mirabel, P., George, C. (1998). Uptake rate measurements of
818   methanesulfonic acid and glyoxal by aqueous droplets. J. Phys. Chem. A. 102(3),

819   593-600.

820   Stavarakou, T., Müller, J.-F., De Smedt, I., Van Roozendael, M., Kanakidou, M.,
821   Vrekoussis, M., Wittrock, F., Richter, A., Burrows, J.P., 2009. The continental
822   source of glyoxal estimated by the synergistic use of spaceborne measurements
823   and inverse modelling. Atmos. Chem. Phys. 9, 8431-8446.

824   Stein, A., Woolley, H., Cooper, S. D., Fairburn, C. G., 1994. An Observational Study of
825   Mothers with Eating Disorders and Their Infants. J. Child. Psychol. Psyc.
826   35(4), 733-748.

827   Steinfeld., Jeffrey, I., 1998. Atmospheric chemistry and physics: from air pollution to
828   climate change. Sci. Policy. Sustain. Dev. 40(7), 26-26.

829   Sumner, A. J., Woo, J. L., McNeill, V. F., 2014. Model Analysis of secondary organic
830   aerosol formation by glyoxal in laboratory studies: The case for photoenhanced
831   chemistry. Environ. Sci. Technol. 4820, 11919-11925.

832   Volkamer, R., Barnes, I., Platt, U., Molina, L. T., Molina, M. J., 2006. Remote sensing
833   of glyoxal by differential optical absorption spectroscopy (DOAS):
834   Advancements in simulation chamber and field experiments. Environmental
835   Simulation Chambers: Application to Atmospheric Chemical Processes:
836   Springer.

837   Volkamer, R., San Martini, F., Molina, L. T., Salcedo, D., Jimenez, J. L., Molina, M. J.,
838   2007. A missing sink for gas-phase glyoxal in Mexico City: Formation of
839   secondary organic aerosol. Geophys. Res. Lett. 34(19), 255-268.

840   Wang, B. L., Liu, Y., Shao, M., Lu, S. H., Wang, M., Yuan, B., 2016. The contributions
841   of biomass burning to primary and secondary organics: A case study in Pearl
842   River Delta (PRD), China. Sci. Total Environ. 569-570, 548-556.

843   Wang, M., Zeng, L., Lu, S., Shao, M., Liu, X., Yu, X., 2014. Development and
844   validation of a cryogen-free automatic gas chromatograph system (GC-MS/FID)
845   for online measurements of volatile organic compounds. Anal. Methods. 6(23),
846   9424-9434.

847   Wang, S., Wu, D., Wang, X. M., Fung, J. C. H., Yu, J. Z., 2013. Relative contributions
848   of secondary organic aerosol formation from toluene, xylenes, isoprene, and
849   monoterpenes in Hong Kong and Guangzhou in the Pearl River Delta, China:
850   an emission-based box modeling study. J. Geophys. Res. Atmos. 118, 507-519.

851   Waxman, E. M., Elm, J., Kurtén, T., Mikkelsen, K. V., Ziemann, P. J., Volkamer, R.,
852   2015. Glyoxal and methylglyoxal setschenow salting constants in sulfate,
853   nitrate, and chloride solutions: Measurements and Gibbs energies. Environ. Sci.
854   Technol. 4919, 11500-11508.

855   Waxman, E.M., Dzepina, K., Erves, B., Lee-Taylor, J., Aumont, B., Jimenez, J.L.,
856   Madronich, S., Volkamer, R., 2013. Secondary organic aerosol formation from
857   semi- and intermediate volatility organic compounds and glyoxal: relevance of
858   O/C as a tracer for aqueous multiphase chemistry. Geophys. Res. Lett. 40, 978-
859   982.

860   Wang, X.M., 2019. Study on the roles of semi-volatile organic compound in the
861   formation of secondary organic aerosol in East China. NSFC briefing in
862   Guangzhou, China. Page 3.

863   Wang, X.M., Wu, Z.Y., Liang, G.X., 2009. WRF/CHEM modeling of impacts of
864   weather conditions modified by urban expansion on secondary organic aerosol
865   formation over Pearl River Delta. Particuology 7, 384-391.
866   Wang, Y., Wang, H., Guo, H., Lyu, X.P., Cheng, H.R., Ling, Z.H., Louie, P.K.K.,
867   Simpson, I.J., Meinardi, S., Blake, D.R., 2017. Long-term O_3-precursor
868   relationships in Hong Kong: field observation and model simulation. Atmos.
869   Chem. Phys. 17, 10919-10935.
870   Wu, L.Q., Wang, X.M., Lu, S.H., Shao, M., Ling, Z.H., 2019. Emission inventory of
871   semi-volatile and intermediate-volatility organic compounds and their effects
872   on secondary organic aerosol over the Pearl River Delta region. Atmos. Chem.
873   Phys. 19, 8141-8161.
874   Xu, Z., Wang, T., Xue, L. K., Louie, P. K. K., Luk, C. W. Y., Gao, J., 2013. Evaluating
875   the uncertainties of thermal catalytic conversion in measuring atmospheric
876   nitrogen dioxide at four differently polluted sites in China. Atmos. Environ.
877   76(Sp. Iss. SI), 221-226.
878   Xue, L. K., Wang, T., Gao, J., Ding, A. J., Zhou, X. H., Blake, D. R., Wang, X. F.,
879   Saunders, S. M., Fan, S. J., Zuo, H. C., Zhang, Q. Z., Wang, W. X., 2014a.
880   Ground-level ozone in four Chinese cities: precursors, regional transport and
881   heterogeneous processes. Atmos. Chem. Phys. (14)23, 13175-13188.
882   Xue, L. K., Wang, T., Louie, P. K. K., Luk, C. W. Y., Blake, D. R., Xu, Z., 2014b.
883   Increasing external effects negate local efforts to control ozone air pollution: a
884   case study of Hong Kong and implications for other Chinese cities. Environ. Sci.
885   Technol. 48(18), 10769-10775.
886   Yun, H., Wang, W., Wang, T., Xia, M., Yu, C., Wang, Z., Poon, S. C. N., Yue, D., Zhou,
887   Y., 2018. Nitrate formation from heterogeneous uptake of dinitrogen pentoxide
888   during a severe winter haze in southern China. Atmos. Chem. Phys. 18(23),
889   17515-17527.
890   Zhang, R.Y., Wang, G.H., Guo, S., Zamora, M.L., Ying, Q., Lin, Y., Wang, W.G., Hu,
891   M., Wang, Y., 2015. Formation of urban fine particle matter. Chem. Rev. 115,
892   3803-3855.
893   Zhang, Y. L., Wang, X. M., Sheng, W., Herrmann, H., Yang, W. Q., Huang, X. Y., Zhou,
894   Z., Huang, Z. H., He, Q. F., George, C., 2016. On-road vehicle emissions of
895   glyoxal and methylglyoxal from tunnel tests in urban Guangzhou, China. Atmos.
896   Environ. 127 55-60.
897   Zhang, Z., Wang, H., Chen, D., Li, Q., Thai, P., Gong, D., 2017. Emission
898   characteristics of volatile organic compounds and their secondary organic
899   aerosol formation potentials from a petroleum refinery in pearl river delta, china.
900   Science of The Total Environment. Sci. Total Environ. 584-585, 1162.
901   Zhou, X., Mopper, K., 1990. Measurement of sub-parts-per-billion levels of carbonyl
902   compounds in marine air by a simple cartridge trapping procedure followed by
903   liquid chromatography. Environ. Sci. Technol. 24(10), 1482-1485.
904   Zhou, Y, Zhong, LJ, Yue, DL, Zeng, LM, Zhang, T. 2014. Potential ozone formation
905   and emission sources of atmospheric VOCs in Heshan during typical pollution
906   episode. Environ. Monit. Forewarning. 6 1-5.

907   Zhou, Y., Yue, DL, Zhong, LJ, Zeng, LM. 2013. Properties of atmospheric PAN
908   pollution in Heshan during summer time. Admin. Tech. Environ. Monitor. 4 24-
909   27.
910   Zhu, T., Shang, J., Zhao, D. F., 2011. The roles of heterogeneous chemical processes in
911   the formation of an air pollution complex and gray haze. Sci. China. Chem.
912   54(1), 145-153.
913
914
915